Delicate Ferromagnetism in MnBi$_6$Te$_{10}$

Chenhui Yan, Yanglin Zhu, Leixin Miao, Sebastian Fernandez-Mulligan, Emanuel Green, Ruobing Mei, Hengxin Tan, Binghai Yan, Chao-Xing Liu, Nasim Alem, Zhiqiang Mao, and Shuolong Yang*

ACCESS | Metrics & More | Article Recommendations | SI Supporting Information

ABSTRACT: Tailoring magnetic orders in topological insulators is critical to the realization of topological quantum phenomena. An outstanding challenge is to find a material where atomic defects lead to tunable magnetic orders while maintaining a nontrivial topology. Here, by combining magnetization measurements, angle-resolved photoemission spectroscopy, and transmission electron microscopy, we reveal disorder-enabled, tunable magnetic ground states in MnBi$_6$Te$_{10}$. In the ferromagnetic phase, an energy gap of 15 meV is resolved at the Dirac point on the MnBi$_2$Te$_4$ termination. In contrast, antiferromagnetic MnBi$_6$Te$_{10}$ exhibits gapless topological surface states on all terminations. Transmission electron microscopy and magnetization measurements reveal substantial Mn vacancies and Mn migration in ferromagnetic MnBi$_6$Te$_{10}$. We provide a conceptual framework where a cooperative interplay of these defects drives a delicate change of overall magnetic ground state energies and leads to tunable magnetic topological orders. Our work provides a clear pathway for nanoscale defect-engineering toward the realization of topological quantum phases.

KEYWORDS: magnetic topological insulator, MnBi$_6$Te$_{10}$, ferromagnetism, antiferromagnetism, defects
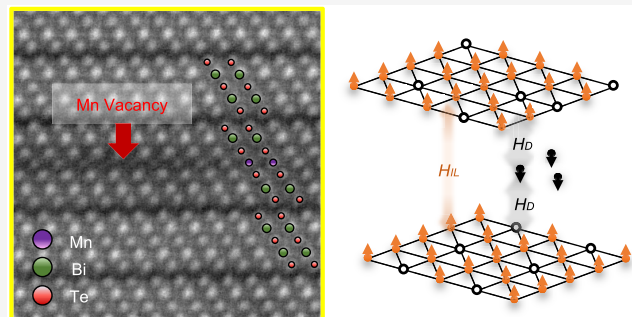
T he first intrinsic magnetic topological insulator MnBi$_2$Te$_4$ (MBT)[1−16] integrates topology with magnetism, and provides a fertile ground for realizing fascinating topological phases. Importantly, MBT exhibits intralayer ferromagnetism and interlayer antiferromagnetism. The compensated magnetic moments in even-layer MBT and the uncompensated ones in odd-layer counterparts give rise to axion insulators[1] and quantum anomalous Hall (QAH) insulators,[14] respectively. The key to tuning and optimizing these topological phases is to precisely control the interlayer magnetic interactions.

A promising route is to construct MnBi$_{2n}$Te$_{3n+1}$ super-lattices, where Bi$_2$Te$_3$ (BT) buffer layers are inserted between the MBT layers. Previous studies have revealed that super-lattices with $n \leq 3$ exhibit interlayer antiferromagnetism,[17−23] whereas those with $n > 3$ display ferromagnetism.[23−25] On the other hand, for higher order superlattices the interlayer magnetic interactions become progressively weaker,[23] which puts a strong limit on the tunability of magnetic interactions and subsequently on the onset temperatures of the resulting topological phases. Notably, previous studies on powder MnBi$_6$Te$_{10}$[26] or hydrostatically pressurized MnBi$_6$Te$_{10}$[27] revealed the possibility of tunable magnetic ground states, yet the nature of these samples disallowed angle-resolved photoemission spectroscopy (ARPES) to directly determine the band topology.

An alternative route is to explore the prevalent disorder effects in MBT and related compounds,[28−33] and potentially use disorder to control the interlayer magnetic interactions.

Recent experiments on MnSb$_2$Te$_4$ (MST) and Sb-doped MnBi$_{2n}$Te$_{3n+1}$ have demonstrated that the Mn/Sb and Mn/Bi antisite defects play an important role in tuning the system between antiferromagnetic (AFM) and ferromagnetic (FM) phases.[29,34] However, no direct evidence has been found in the momentum space for the broken-symmetry gap in these materials. Moreover, the topological nature of MST is still under intense debates due to the reduced spin−orbit coupling (SOC) effect.[12,35,36] It is thus an intriguing question whether such disorder-mediated magnetic interactions can be realized in the MBT-derived compounds without compromising the SOC effect, which potentially enables tunable topological phases by a sensitive control of the disorder.

In this Letter, we report a delicate FM topological insulator state in MnBi$_6$Te$_{10}$, which is attributed to disorder-mediated magnetic interactions. We employ high-resolution laser-based ARPES to detail the electronic structures of the FM and AFM phases, respectively. In the FM phase, a broken-symmetry gap is unambiguously observed on the topological surface state (TSS) of the MBT termination, with a gap onset temperature
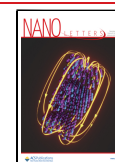
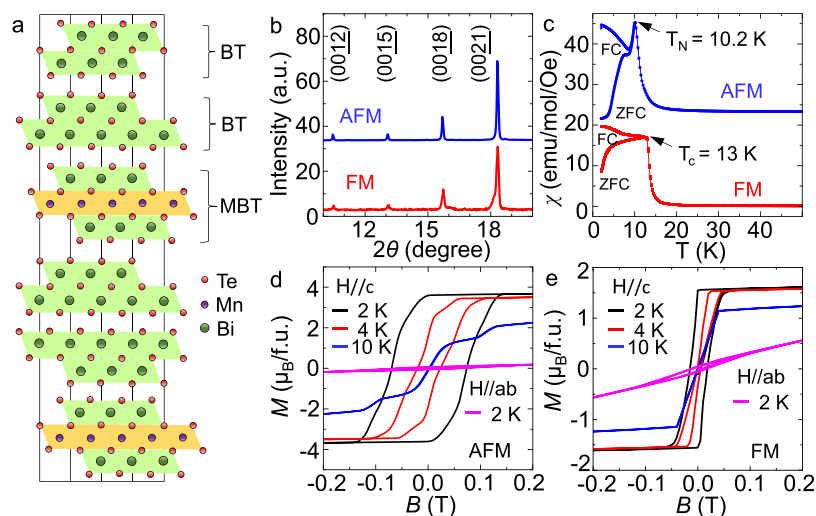**Figure 1.** Structural and magnetic characterizations of $MnBi_6Te_{10}$. (a) Schematic crystal structure of $MnBi_6Te_{10}$. (b) X-ray diffraction of ferromagnetic (FM, red) and antiferromagnetic (AFM, blue) $MnBi_6Te_{10}$. (c) Temperature dependent zero-field-cooled (ZFC) and field-cooled (FC) magnetic susceptibilities of FM (red) and AFM (blue) $MnBi_6Te_{10}$ using an external field $H = 100$ Oe along the c-axis. The results corresponding to the AFM samples are offset vertically for clarity. (d,e) Isothermal magnetization curves with the magnetic field applied along the c-axis and in the ab plane at various temperatures in (d) AFM and (e) FM $MnBi_6Te_{10}$.
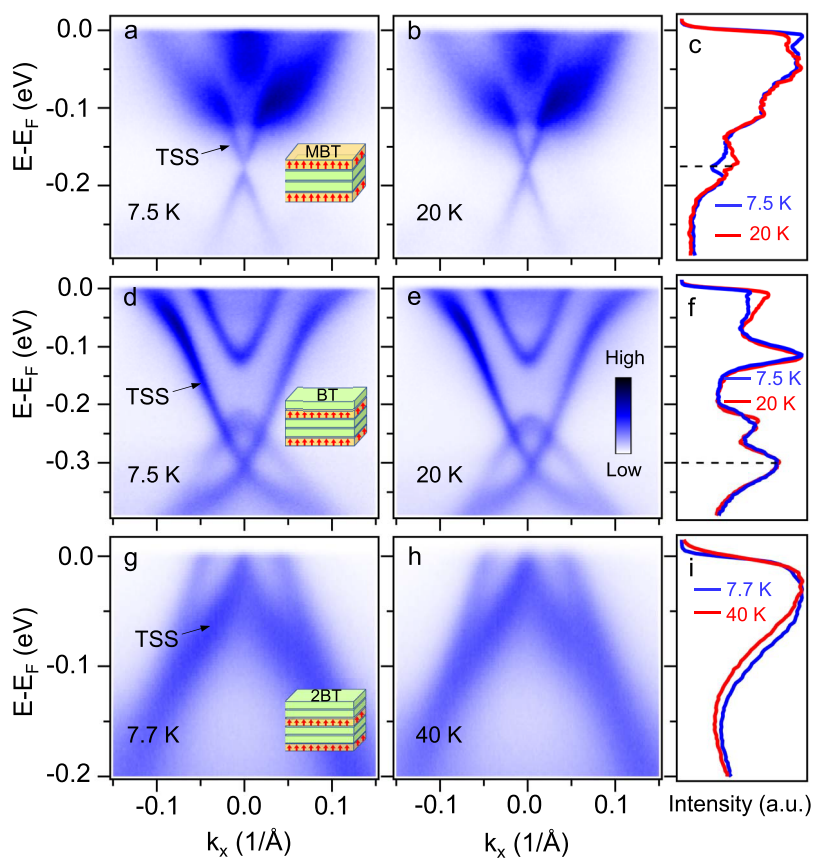

Figure 2. Electronic structure of ferromagnetic $MnBi_6Te_{10}$. Energy-momentum spectra along $\overline{\Gamma} - \overline{M}$ at (a) 7.5 K, and (b) 20 K. The insert in (a) illustrates the $MnBi_2Te_4$ (MBT) termination. (c) Comparison of energy distribution curves at $\overline{\Gamma}$. An energy gap is observed at the Dirac point (black dashed line) at 7.5 K. The counterpart results for the 1-Bi_2Te_3 (1-BT) termination are plotted in (d−f): (d,e) energy-momentum spectra, and (f) energy distribution curves at $\overline{\Gamma}$. The counterpart results for the 2-Bi_2Te_3 (2-BT) termination are plotted in (g−i): (g,h) energy-momentum spectra, and (i) energy distribution curves at $\overline{\Gamma}$.

coinciding with the Curie temperature. In stark contrast, all terminations of the AFM phase of $MnBi_6Te_{10}$ exhibit negligible energy gaps on the TSS. Furthermore, our structural and magnetic characterizations reveal that Mn vacancies in MBT

layers and Mn migration from MBT to BT layers are prevalent in FM $MnBi_6Te_{10}$. We provide a conceptual framework where a delicate interplay of Mn vacancies and Mn migration leads to the tunable magnetic phases in $MnBi_6Te_{10}$. Our work not only

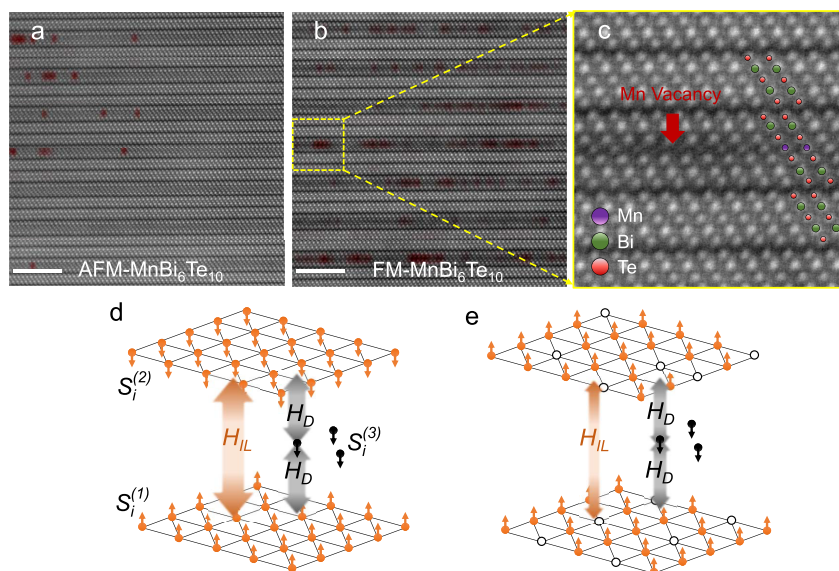**Figure 3.** Structural characterizations of $MnBi_6Te_{10}$. Annular dark-field scanning transmission electron microscopy (ADF-STEM) images of (a) AFM and (b) FM $MnBi_6Te_{10}$. Scale bar indicates 5 nm. Mn vacancies are highlighted by red shading, where the intensity for the atomic column of Mn is lower than the value of two standard deviations below the Mn mean intensity. (c) Magnified image (yellow box in (b)). (d) A cartoon illustration showing $H_{IL} > H_D$ in the AFM phase. (e) With increased Mn vacancies, $H_{IL} < H_D$ in the FM phase.

establishes the first unequivocal FM topological insulator phase in $MnBi_6Te_{10}$, but also demonstrates one of the highest FM T_c's (13 K) among all MBT-derived compounds.[24,25,37] The proposed new scheme of disorder-mediated ferromagnetism provides a pathway toward sensitive nanoscale tuning of topological phases and future topological quantum devices.

The $MnBi_6Te_{10}$ single crystals were synthesized through a self-flux method.[20] So far, only the AFM phase was reported in $MnBi_6Te_{10}$, which is the ground state for $MnBi_{2n}Te_{3n+1}$ ($n \leq$ 3). The FM phase has 0.05 meV higher total energy per Mn atom that may be compensated by introducing certain type of defects.[23,38] To meet this challenge, we increased the growth temperature window by 5 °C for FM samples comparing with the growth temperature for AFM samples in order to create Mn/Bi antisites and Mn vacancies, as both types of defects can weaken the interlayer AFM exchange coupling.

As shown in Figure 1b, the X-ray diffraction (XRD) patterns for the two magnetic phases exhibit the same $(00l)$ diffraction peaks in good agreement with previous studies.[20,39,40] Figure 1c displays the zero-field-cooled (ZFC) and field-cooled (FC) magnetic susceptibilities measured with a c-axis applied field H = 100 Oe. A sharp Λ-like peak at 10.2 K is observed in the magnetic susceptibility of AFM $MnBi_6Te_{10}$, which indicates an AFM transition.[20,23,25] The ZFC-FC bifurcation below 8 K seen in the AFM sample can be attributed to the evolution from a long-range AFM order to a cluster spin glass state,[23] which is likely driven by the magnetic frustration caused by competing FM and AFM interactions. In contrast, the magnetic susceptibility for the FM material shows signatures of a typical FM transition: a rapid increase and plateauing of the susceptibility below the Curie temperature of 13 K. For FM MBT-derived materials, magneto-optical imaging has demonstrated that the ZFC-FC bifurcation in magnetic susceptibilities is likely due to the movement of FM domains.[41] The FM phase is further confirmed by the isothermal magnetization curves in Figure 1e: a typical hysteresis loop expected for FM materials is revealed. In contrast, a spin-flop-

like transition is observed in the AFM phase (Figure 1d), in agreement with previous reports on AFM $MnBi_4Te_7$.[19]

High-resolution ARPES results on FM $MnBi_6Te_{10}$ are presented in Figure 2. Three possible terminations are expected after cleaving, denoted by the top layer as MBT, single BT (1-BT), or double BT (2-BT) terminations. It is crucial to employ micron-scale laser beams to distinguish different terminations. Figure 2 presents three types of electronic structures found on FM $MnBi_6Te_{10}$. First, we point out that the termination assignment cannot be based on direct comparison between ARPES data and first-principles calculations, as the latter is often unable to properly model the impacts of defects and quantum confinement in $MnBi_{2n}Te_{3n+1}$ materials.[16,40,42] A common spectroscopic feature characteristic of the MBT termination for all $MnBi_{2n}Te_{3n+1}$ superlattices is a Dirac surface state hybridized with parabolic Rashba bands.[16,40,43] Hence, we associate the electronic structure in Figure 2a with the MBT termination. We assign the spectrum in Figure 2d to the 1-BT termination due to its strong resemblance with the counterpart on the 1-BT termination of FM $Mn(Bi_{0.85}Sb_{0.15})_4Te_7$.[37] Finally, since our material is phase-pure as demonstrated by the transmission electron microscopy measurement (Figure 3), we can only assign the last type of ARPES spectrum (Figure 2g) to the 2-BT termination. The two different types of BT-derived terminations exhibit electron (Figure 2d) and hole (Figure 2g) dopings, respectively. We notice that the qualitative trend is consistent with the previous ARPES data on the BT-derived terminations of AFM $MnBi_6Te_{10}$[40] and FM $MnBi_8Te_{13}$,[25] where electron doping systematically decreases as the number of BT layers increases. Nevertheless, the doping change from the 1-BT to the 2-BT terminations in FM $MnBi_6Te_{10}$ is much more dramatic, which may be due to its specific defect configuration [Supporting Information (SI) Note 1].

We focus on the MBT and 1-BT terminations as their Dirac points are clearly resolvable below the Fermi level. Circular dichroism in ARPES measurements exhibits antisymmetric patterns near the Dirac point for both terminations (SI Figure

1). A helical circular dichroism (CD) pattern in ARPES has been successfully used to identify the topological surface state in $MnBi_{2n}Te_{3n+1}$ compounds.[11,43] For the MBT termination, an energy gap of ~15 meV at the Dirac point is visible in the ARPES data at 7.5 K and this gap disappears at 20 K (Figure 2a,b). The comparison of energy distribution curves (EDCs) taken at $\bar{\Gamma}$ further highlights this temperature-dependent energy gap: a spectral peak at −0.18 eV at 20 K evolves into a dip upon cooling to 7.5 K. A temperature-dependent band dispersion analysis on the MBT termination yields a gap-closing temperature at 12.7 ± 1.4 K (SI Note 2 and SI Figure 2), yet we cannot completely rule out the existence of a finite gap above T_c. For the 1-BT termination, the spectra taken at both temperatures exhibit gapless Dirac cones (Figure 2d−f).

AFM $MnBi_6Te_{10}$ exhibits three types of ARPES spectra on three terminations (SI Figure 3 and SI Figure 4).[21,40,44,45] The energy gaps at the Dirac points are negligible on all terminations of AFM $MnBi_6Te_{10}$, consistent with previous reports.[22,40,43] While it is not the focus of our work, we point out that a likely scenario for the gapless TSS on the MBT termination of AFM $MnBi_6Te_{10}$ is that the Mn−Bi antisite defects may cause the TSS wave function to be relocated into the space between two adjacent MBT septuple layers.[46] Both the nonmagnetic BT layers and the opposite magnetic moments from the two adjacent MBT layers may reduce the magnetic gap.

We thus establish the spectroscopic evidence of a magnetically induced broken-symmetry gap in FM $MnBi_6Te_{10}$ for the first time. This gap originates from strong interactions between the TSS electrons and the magnetic moments in the MBT layer. In contrast, the TSS electrons on the 1-BT termination are localized to the top BT layer and spatially separate from the magnetic MBT layer, leading to a gapless Dirac point. Gap opening in the $MnBi_{2n}Te_{3n+1}$ compound family has been highly controversial.[2,3,6,7,11,16,22,23,25,40,44,47−50] Specifically on $MnBi_6Te_{10}$, a 60 meV gap was reported in the AFM phase[44] in contrast to the results from all other ARPES studies on $MnBi_6Te_{10}$[22,23,25,40] including ours. However, this gap persists well above the magnetic ordering temperature and is likely due to extrinsic reasons such as local impurities. On the contrary, our clear spectroscopic gap in FM $MnBi_6Te_{10}$ which onsets at the magnetic ordering temperature clarifies the physics picture of a broken time-reversal symmetry. In addition, our resolved gap in FM $MnBi_6Te_{10}$ is fully consistent with previous observations on FM $MnBi_8Te_{13}$.[24,25] The crucial new discovery is that the magnetic phase of $MnBi_6Te_{10}$ can be controllably tuned between AFM and FM.

We proceed to investigate the microscopic mechanism leading to tunable magnetic phases. Notably, Mn-doped BT can host ferromagnetism,[51−54] yet the distinct XRD and ARPES results from our FM $MnBi_6Te_{10}$ compared to those from Mn-doped BT[51−53] suggest that the proportion of the latter phase in our materials is negligible. Furthermore, structural characterizations by annular dark field scanning transmission electron microscopy (ADF-STEM) do not find any observable impurity phases for AFM or FM samples, as shown in Figure 3. The atomic resolution images exhibit an interleaved structure composed of MBT septuple layers and 2 BT quintuple layers, which is consistent with the crystal structures determined by XRD in Figure 1b. The selected-area electron diffraction (SAED) patterns, determined by the atomic stacking sequences and periodicity along the c-axis

(SI Figure 5), further confirm the single phase of the FM and AFM $MnBi_6Te_{10}$ samples.

Mn vacancies are observed in both AFM and FM $MnBi_6Te_{10}$, as highlighted in red in Figure 3a−c. Strikingly, the concentration of Mn vacancies in the FM samples (Figure 3b) is much higher than that in the AFM samples (Figure 3a). The quantitative percentages of Mn vacancies are hard to determine from ADF-STEM since the intensity is formed by atoms in the projection of the entire atomic columns perpendicular to the imaging plane. The energy dispersive X-ray (EDX) analysis confirms the higher concentration of Mn vacancies in the FM samples (SI Table 1).

Another important type of disorder is Mn migration. This effect is manifested as the ferrimagnetic order induced by the "antisite defects" in $MnSb_2Te_4$[28,29] and Sb-doped $MnBi_4Te_7$.[34,55] Measurements of magnetic moments at low and high magnetic fields can be used to estimate the density of Mn migration.[32] Using our measured magnetic moments at 0.2 T (Figure 1) and 7 T (SI Figure 6), we obtain that 8.1% and 11.8% of Mn atoms in FM and AFM $MnBi_6Te_{10}$, respectively, have migrated from the original Mn sheets to the neighboring layers. Here we use the chemical formula of $Mn_{1−y−6x}(Bi_{1−x}Mn_x)_6Te_{10}$, where $6x$ and y indicate the densities of Mn migration and Mn vacancies, respectively. The comparable densities of Mn migration in FM and AFM $MnBi_6Te_{10}$ suggest that the true physical picture for the FM order is more complex than a simple migration-induced ferrimagnetism.[29]

We construct a conceptual model to illustrate that it is the delicate interplay of Mn vacancies and Mn migration that leads to the tunable magnetic phases in $MnBi_6Te_{10}$. We consider two Mn sheets where the intralayer and interlayer magnetic interactions are FM and AFM, respectively. An intermediate layer of migrated Mn ions interacts with the original Mn sheets antiferromagnetically. We obtain the energy difference between the FM and AFM alignments of the original Mn sheets (SI Note 3)

$$E_{FM} - E_{AFM} = 2 \sum_{i,j}^{(1),(2)} J_{IL,ij} - 2 \sum_{i,j}^{(1),(3)} J_{D,ij} = 2H_{IL} - 2H_D$$

(1)

Here $J_{IL,ij}$ is the interlayer magnetic coupling between site i and j in the two original Mn sheets; $J_{D,ij}$ is the defect-induced magnetic coupling across the original Mn sheets and the defect layer. Importantly, the scenarios of $H_{IL} > H_D$ and $H_{IL} < H_D$ lead to the AFM and FM alignment of the two original Mn sheets, respectively.

To evaluate the energy balance in the presence of Mn vacancies and Mn migration, we consider the scaling laws of H_{IL} and H_D in terms of the Mn density in the original sheets (n_o) and in the migrated space (n_m): $H_{IL} \propto n_o^2$ and $H_D \propto n_o n_m$. These scaling laws are rooted in the microscopic nature of magnetic interactions (SI Note 4), and independent of the numerical details of $J_{D,ij}$ and $J_{IL,ij}$. Subsequently

$$H_D/H_{IL} \propto n_m/n_o$$

(2)

Equation 2 reveals the microscopic mechanism for defect-induced ferromagnetism in $MnBi_6Te_{10}$. First, with substantial Mn vacancies in the MBT layer, both H_{IL} and H_D decrease (Figure 3e). The energy balance is determined by n_m/n_o. Notably, the saturated magnetic moments at low and high magnetic fields (M_1 and M_2, respectively) allow us to estimate

this ratio:[32] $n_m/n_o = (M_2 - M_1)/(M_2 + M_1)$. Our measurements lead to $n_m/n_o = 0.2$ and 0.13 for the FM and AFM samples, respectively (SI Note 4). The values of n_m/n_o for all the AFM $MnBi_6Te_{10}$ materials in the literature are smaller than 0.1.[20,25,38] The > 50% increase of n_m/n_o tips the energy balance between H_D and H_{IL}, stabilizing a ferromagnetic phase (Figure 3e). We remark that the more accurate n_m/n_o can be >0.2 for FM $MnBi_6Te_{10}$ due to the potentially unsaturated M_2 at 7 T.[32]

We emphasize that the simple Ising model neglects other types of magnetic interactions and should only serve as a conceptual framework. Nevertheless, it offers powerful scaling laws under which the delicate adjustment of Mn vacancies and Mn migration leads to tunable magnetic phases in $MnBi_6Te_{10}$. We emphasize that this disorder tuning leads to a change of the "global" magnetic ground state, which is to be distinguished from the more trivial disorder effect resulting in local changes of magnetism.[36] Our new insight of quantitatively considering the ratio of n_m/n_o is a substantial advance compared to previous studies which qualitatively pointed out the importance of disorder[36,56] and the theoretical modeling whose predictions sensitively depend on numerical details.[55] This insight, importantly, is obtained by the multimodal measurements combining magnetization, laser-based μARPES, and atomic-resolution TEM on the same batch of samples. Notably, FM $MnBi_6Te_{10}$ exhibits a T_c of 13 K, which is higher than the T_c of 10.5 K for FM $MnBi_8Te_{13}$[24,25] and the T_c < 9 K for hydrostatically pressured $MnBi_6Te_{10}$,[27] suggesting that the disorder-induced ferromagnetism may be more robust than that induced by superlattice stacking or by hydrostatic pressure. The delicate ferromagnetism revealed in this work will serve as a general framework to understand the phenomenology in all $MnBi_{2n}Te_{3n+1}$ superlattices.

We hope that our work will serve as a milestone to motivate further theoretical and experimental studies, in particular spectroscopy and microscopy studies with atomic resolutions to resolve what defects form under what growth conditions in disordered FM $MnBi_{2n}Te_{3n+1}$. The defect engineering via controlling the growth temperature can potentially be adapted in thin film deposition of $MnBi_{2n}Te_{3n+1}$ as well. Understanding how to tune the magnetism and topological states without introducing new chemical elements in the same MBT system through delicately controlling the defects, allows us to selectively realize exotic phases such as the axion insulator state and the quantum anomalous Hall insulator state, paving the road toward functional topological quantum devices at realistic cryogenic temperatures.

METHODS

Sample Growth and Characterization. $MnBi_6Te_{10}$ single crystals were synthesized using the self-flux method,[20] in which Mn, Bi, and Te powders were mixed with a stoichiometric molar ratio and sealed in a carbon-coated quartz tube under high vacuum. For the synthesis of ferromagnetic (FM) $MnBi_6Te_{10}$, the mixture was heated to 900 °C in a furnace and held for 10 h for homogeneous melting. The mixture then underwent a series of cooling and annealing stages: from 900 to 595 °C in 5 h, from 595 to 580 °C at a rate of 0.1 °C/h, annealed at 580 °C for 48 h, and finally quenched in water at 0 °C. For the synthesis of antiferromagnetic (AFM) $MnBi_6Te_{10}$, the same melting was adopted. It was followed by cooling from 900 to 590 °C in 5 h and then from 590 to 575 °C at a rate of 0.1 °C/h, annealed at 575 °C for 48 h and then

quenched in water at 0 °C. The as-grown single crystals were found to be plate-like with luster and lateral dimensions of 2 × 2 mm².

The crystallization of the grown single crystals was verified by the sharp (00L) XRD peaks using a Malvern Panalytical Empyrean diffractometer (Cu K$_\alpha$ radiation), as shown in Figure 1b. Magnetization of crystals was measured by the MPMS3 SQUID magnetometer (Quantum Design).

The TEM specimens were prepared using ThermoFisher Helios 660 dual beam system. The specimens were thinned down to electron transparency using 30 kV and 5 kV Ga ion beam and cleaned with 2 kV and 1 kV ion beam. The aberration-corrected STEM imaging was performed using ThermoFisher Titan G2 S/TEM equipped with image and probe correctors. The operating voltage for the STEM imaging was 200 kV. The STEM images have been drift corrected using the nonlinear drift correction algorithm. The elemental mapping was acquired with energy dispersive X-ray spectroscopy (EDS) with STEM mode.

Ultrahigh Resolution Laser-Based Angle-Resolved Photoemission Spectroscopy (ARPES). Our laser-based ARPES setup was based on a Coherent MIRA Ti:sapphire oscillator. With a 5 W, 532 nm continuous wave seed laser, the oscillator output >9 nJ pulses with a central wavelength at 820 nm, a bandwidth of 7.6 nm, a pulse duration of 130 fs, and a repetition rate of 80 MHz. One mm beta barium borate (BBO) crystals were used to generate the second harmonic (410 nm) and fourth harmonic (205 nm), the latter of which was used for ARPES measurements. The optical bandwidth of the 6 eV beam was expected to be 2.7 meV due to the finite BBO thicknesses. The overall energy resolution incorporating the ARPES analyzer resolution was characterized as 4 meV.[57] The beam waist at the optical focal point was less than 10 μm.[57]

ASSOCIATED CONTENT

SI Supporting Information

The Supporting Information is available free of charge at https://pubs.acs.org/doi/10.1021/acs.nanolett.2c02500.

Defects and doping, circular dichroism in the ARPES spectra of ferromagnetic $MnBi_6Te_{10}$, side-by-side comparison of FM and AFM $MnBi_6Te_{10}$ using the temperature evolutions of the TSS's on the MBT termination, electronic structure of antiferromagnetic $MnBi_6Te_{10}$, circular dichroism in the ARPES spectra of antiferromagnetic $MnBi_6Te_{10}$, selected area electron diffraction (SAED) patterns of $MnBi_6Te_{10}$, high-field magnetization measurements of AFM and FM $MnBi_6Te_{10}$, estimates of the chemical concentrations of $MnBi_6Te_{10}$ based on the scanning transmission electron microscopy−energy dispersive X-ray (STEM-EDX) analysis, magnetic interactions, and the determination of the Mn density ratio between different layers (PDF)

AUTHOR INFORMATION

Corresponding Author

Shuolong Yang − *Pritzker School of Molecular Engineering, University of Chicago, Chicago, Illinois 60637, United States;* ● orcid.org/0000-0002-8200-9898; Email: yangsl@uchicago.edu

Authors

Chenhui Yan − *Pritzker School of Molecular Engineering, University of Chicago, Chicago, Illinois 60637, United States;* ◉ orcid.org/0000-0002-5440-9536

Yanglin Zhu − *Department of Physics, Pennsylvania State University, State College, Pennsylvania 16802, United States*

Leixin Miao − *Department of Materials Science and Engineering, The Pennsylvania State University, State College, Pennsylvania 16802, United States*

Sebastian Fernandez-Mulligan − *Pritzker School of Molecular Engineering, University of Chicago, Chicago, Illinois 60637, United States*

Emanuel Green − *Pritzker School of Molecular Engineering, University of Chicago, Chicago, Illinois 60637, United States*

Ruobing Mei − *Department of Physics, Pennsylvania State University, State College, Pennsylvania 16802, United States*

Hengxin Tan − *Department of Condensed Matter Physics, Weizmann Institute of Science, Rehovot 7610001, Israel*

Binghai Yan − *Department of Condensed Matter Physics, Weizmann Institute of Science, Rehovot 7610001, Israel;* ◉ orcid.org/0000-0003-2164-5839

Chao-Xing Liu − *Department of Physics, Pennsylvania State University, State College, Pennsylvania 16802, United States*

Nasim Alem − *Department of Materials Science and Engineering, The Pennsylvania State University, State College, Pennsylvania 16802, United States;* ◉ orcid.org/0000-0003-0009-349X

Zhiqiang Mao − *Department of Physics, Pennsylvania State University, State College, Pennsylvania 16802, United States*

Complete contact information is available at:
https://pubs.acs.org/10.1021/acs.nanolett.2c02500

Author Contributions

C.Y., S.M., E.G., and S.Y. performed the ARPES measurements. Y.Z. and Z.M. grew the samples and performed the magnetization measurements. L.M. and N.A. performed the STEM measurements. All authors discussed the results and commented on the paper. C.Y. and S.Y. wrote the paper with input from all authors.

Notes

The authors declare no competing financial interest.

■ REFERENCES

(1) Liu, C.; Wang, Y.; Li, H.; Wu, Y.; Li, Y.; Li, J.; He, K.; Xu, Y.; Zhang, J.; Wang, Y. Robust Axion Insulator and Chern Insulator Phases in a Two-Dimensional Antiferromagnetic Topological Insulator. *Nat. Mater.* **2020**, *19*, 522.

(2) Otrokov, M. M.; Klimovskikh, I. I.; Bentmann, H.; Estyunin, D.; Zeugner, A.; Aliev, Z. S.; Gaß, S.; Wolter, A. U. B.; Koroleva, A. V.; Shikin, A. M.; Blanco-Rey, M.; Hoffmann, M.; Rusinov, I. P.; Vyazovskaya, A. Y.; Eremeev, S. V.; Koroteev, Y. M.; Kuznetsov, V. M.; Freyse, F.; Sánchez-Barriga, J.; Amiraslanov, I. R.; Babanly, M. B.; Mamedov, N. T.; Abdullayev, N. A.; Zverev, V. N.; Alfonsov, A.; Kataev, V.; Büchner, B.; Schwier, E. F.; Kumar, S.; Kimura, A.; Petaccia, L.; Di Santo, G.; Vidal, R. C.; Schatz, S.; Kißner, K.; Ünzelmann, M.; Min, C. H.; Moser, S.; Peixoto, T. R. F.; Reinert, F.; Ernst, A.; Echenique, P. M.; Isaeva, A.; Chulkov, E. V. Prediction and Observation of an Antiferromagnetic Topological Insulator. *Nature* **2019**, *576* (7787), 416−422.

(3) Rienks, E. D. L.; Wimmer, S.; Sánchez-Barriga, J.; Caha, O.; Mandal, P. S.; Růžička, J.; Ney, A.; Steiner, H.; Volobuev, V. V.; Groiss, H.; Albu, M.; Kothleitner, G.; Michalička, J.; Khan, S. A.; Minár, J.; Ebert, H.; Bauer, G.; Freyse, F.; Varykhalov, A.; Rader, O.; Springholz, G. Large Magnetic Gap at the Dirac Point in Bi_2Te_3/$MnBi_2Te_4$ Heterostructures. *Nature* **2019**, *576* (7787), 423−428.

(4) Gong, Y.; Guo, J.; Li, J.; Zhu, K.; Liao, M.; Liu, X.; Zhang, Q.; Gu, L.; Tang, L.; Feng, X.; Zhang, D.; Li, W.; Song, C.; Wang, L.; Yu, P.; Chen, X.; Wang, Y.; Yao, H.; Duan, W.; Xu, Y.; Zhang, S.-C.; Ma, X.; Xue, Q.-K.; He, K. Experimental Realization of an Intrinsic Magnetic Topological Insulator. *Chin. Phys. Lett.* **2019**, *36* (7), 076801.

(5) Zeugner, A.; Nietschke, F.; Wolter, A. U. B.; Gaß, S.; Vidal, R. C.; Peixoto, T. R. F.; Pohl, D.; Damm, C.; Lubk, A.; Hentrich, R.; Moser, S. K.; Fornari, C.; Min, C. H.; Schatz, S.; Kißner, K.; Ünzelmann, M.; Kaiser, M.; Scaravaggi, F.; Rellinghaus, B.; Nielsch, K.; Hess, C.; Büchner, B.; Reinert, F.; Bentmann, H.; Oeckler, O.; Doert, T.; Ruck, M.; Isaeva, A. Chemical Aspects of the Candidate Antiferromagnetic Topological Insulator $MnBi_2Te_4$. *Chem. Mater.* **2019**, *31* (8), 2795−2806.

(6) Swatek, P.; Wu, Y.; Wang, L.-L.; Lee, K.; Schrunk, B.; Yan, J.; Kaminski, A. Gapless Dirac Surface States in the Antiferromagnetic Topological Insulator $MnBi_2Te_4$. *Phys. Rev. B* **2020**, *101* (16), 161109.

(7) Hao, Y.-J.; Liu, P.; Feng, Y.; Ma, X.-M.; Schwier, E. F.; Arita, M.; Kumar, S.; Hu, C.; Lu, R.; Zeng, M.; Wang, Y.; Hao, Z.; Sun, H.-Y.; Zhang, K.; Mei, J.; Ni, N.; Wu, L.; Shimada, K.; Chen, C.; Liu, Q.; Liu, C. Gapless Surface Dirac Cone in Antiferromagnetic Topological Insulator $MnBi_2Te_4$. *Phys. Rev. X* **2019**, *9* (4), 041038.

(8) Chen, Y. J.; Xu, L. X.; Li, J. H.; Li, Y. W.; Wang, H. Y.; Zhang, C. F.; Li, H.; Wu, Y.; Liang, A. J.; Chen, C.; Jung, S. W.; Cacho, C.; Mao, Y. H.; Liu, S.; Wang, M. X.; Guo, Y. F.; Xu, Y.; Liu, Z. K.; Yang, L. X.; Chen, Y. L. Topological Electronic Structure and Its Temperature Evolution in Antiferromagnetic Topological Insulator $MnBi_2Te_4$. *Phys. Rev. X* **2019**, *9* (4), 041040.

(9) Li, H.; Gao, S.-Y.; Duan, S.-F.; Xu, Y.-F.; Zhu, K.-J.; Tian, S.-J.; Gao, J.-C.; Fan, W.-H.; Rao, Z.-C.; Huang, J.-R.; Li, J.-J.; Yan, D.-Y.; Liu, Z.-T.; Liu, W.-L.; Huang, Y.-B.; Li, Y.-L.; Liu, Y.; Zhang, G.-B.; Zhang, P.; Kondo, T.; Shin, S.; Lei, H.-C.; Shi, Y.-G.; Zhang, W.-T.; Weng, H.-M.; Qian, T.; Ding, H. Dirac Surface States in Intrinsic Magnetic Topological Insulators $EuSn_2As_2$ and $MnBi_{2n}Te_{3n+1}$. *Phys. Rev. X* **2019**, *9* (4), 041039.

(10) Vidal, R. C.; Bentmann, H.; Peixoto, T. R. F.; Zeugner, A.; Moser, S.; Min, C.-H.; Schatz, S.; Kißner, K.; Ünzelmann, M.; Fornari,

C. I.; Vasili, H. B.; Valvidares, M.; Sakamoto, K.; Mondal, D.; Fujii, J.; Vobornik, I.; Jung, S.; Cacho, C.; Kim, T. K.; Koch, R. J.; Jozwiak, C.; Bostwick, A.; Denlinger, J. D.; Rotenberg, E.; Buck, J.; Hoesch, M.; Diekmann, F.; Rohlf, S.; Kalläne, M.; Rossnagel, K.; Otrokov, M. M.; Chulkov, E. V.; Ruck, M.; Isaeva, A.; Reinert, F. Surface States and Rashba-Type Spin Polarization in Antiferromagnetic $MnBi_2Te_4$ (0001). *Phys. Rev. B* **2019**, *100* (12), 121104.

(11) Nevola, D.; Li, H. X.; Yan, J.-Q.; Moore, R. G.; Lee, H.-N.; Miao, H.; Johnson, P. D. Coexistence of Surface Ferromagnetism and a Gapless Topological State in $MnBi_2Te_4$. *Phys. Rev. Lett.* **2020**, *125* (11), 117205.

(12) Chen, B.; Fei, F.; Zhang, D.; Zhang, B.; Liu, W.; Zhang, S.; Wang, P.; Wei, B.; Zhang, Y.; Zuo, Z.; Guo, J.; Liu, Q.; Wang, Z.; Wu, X.; Zong, J.; Xie, X.; Chen, W.; Sun, Z.; Wang, S.; Zhang, Y.; Zhang, M.; Wang, X.; Song, F.; Zhang, H.; Shen, D.; Wang, B. Intrinsic Magnetic Topological Insulator Phases in the Sb Doped $MnBi_2Te_4$ Bulks and Thin Flakes. *Nat. Commun.* **2019**, *10*, 4469.

(13) Otrokov, M. M.; Rusinov, I. P.; Blanco-Rey, M.; Hoffmann, M.; Vyazovskaya, A. Yu.; Eremeev, S. V.; Ernst, A.; Echenique, P. M.; Arnau, A.; Chulkov, E. V. Unique Thickness-Dependent Properties of the van Der Waals Interlayer Antiferromagnet $MnBi_2Te_4$ Films. *Phys. Rev. Lett.* **2019**, *122* (10), 107202.

(14) Deng, Y.; Yu, Y.; Shi, M. Z.; Guo, Z.; Xu, Z.; Wang, J.; Chen, X. H.; Zhang, Y. Quantum Anomalous Hall Effect in Intrinsic Magnetic Topological Insulator $MnBi_2Te_4$. *Science* **2020**, *367* (6480), 895−900.

(15) Estyunin, D. A.; Klimovskikh, I. I.; Shikin, A. M.; Schwier, E. F.; Otrokov, M. M.; Kimura, A.; Kumar, S.; Filnov, S. O.; Aliev, Z. S.; Babanly, M. B.; Chulkov, E. V. Signatures of Temperature Driven Antiferromagnetic Transition in the Electronic Structure of Topological Insulator $MnBi_2Te_4$. *APL Mater.* **2020**, *8* (2), 021105.

(16) Yan, C.; Fernandez-Mulligan, S.; Mei, R.; Lee, S. H.; Protic, N.; Fukumori, R.; Yan, B.; Liu, C.; Mao, Z.; Yang, S. Origins of Electronic Bands in the Antiferromagnetic Topological Insulator $MnBi_2Te_4$. *Phys. Rev. B* **2021**, *104* (4), L041102.

(17) Hu, C.; Gordon, K. N.; Liu, P.; Liu, J.; Zhou, X.; Hao, P.; Narayan, D.; Emmanouilidou, E.; Sun, H.; Liu, Y.; Brawer, H.; Ramirez, A. P.; Ding, L.; Cao, H.; Liu, Q.; Dessau, D.; Ni, N. A van Der Waals Antiferromagnetic Topological Insulator with Weak Interlayer Magnetic Coupling. *Nat. Commun.* **2020**, *11*, 97.

(18) Wu, J.; Liu, F.; Sasase, M.; Ienaga, K.; Obata, Y.; Yukawa, R.; Horiba, K.; Kumigashira, H.; Okuma, S.; Inoshita, T.; Hosono, H. Natural van Der Waals Heterostructural Single Crystals with Both Magnetic and Topological Properties. *Sci. Adv.* **2019**, *5* (11), No. eaax9989.

(19) Vidal, R. C.; Zeugner, A.; Facio, J. I.; Ray, R.; Haghighi, M. H.; Wolter, A. U. B.; Corredor Bohorquez, L. T.; Caglieris, F.; Moser, S.; Figgemeier, T.; Peixoto, T. R. F.; Vasili, H. B.; Valvidares, M.; Jung, S.; Cacho, C.; Alfonsov, A.; Mehlawat, K.; Kataev, V.; Hess, C.; Richter, M.; Büchner, B.; van den Brink, J.; Ruck, M.; Reinert, F.; Bentmann, H.; Isaeva, A. Topological Electronic Structure and Intrinsic Magnetization in $MnBi_4Te_7$: A Bi_2Te_3 Derivative with a Periodic Mn Sublattice. *Phys. Rev. X* **2019**, *9* (4), 041065.

(20) Shi, M. Z.; Lei, B.; Zhu, C. S.; Ma, D. H.; Cui, J. H.; Sun, Z. L.; Ying, J. J.; Chen, X. H. Magnetic and Transport Properties in the Magnetic Topological Insulators $MnB_2Te_4(Bi_2Te_3)_n$ (N = 1,2). *Phys. Rev. B* **2019**, *100* (15), 155144.

(21) Tian, S.; Gao, S.; Nie, S.; Qian, Y.; Gong, C.; Fu, Y.; Li, H.; Fan, W.; Zhang, P.; Kondo, T.; Shin, S.; Adell, J.; Fedderwitz, H.; Ding, H.; Wang, Z.; Qian, T.; Lei, H. Magnetic Topological Insulator $MnBi_6Te_{10}$ with a Zero-Field Ferromagnetic State and Gapped Dirac Surface States. *Phys. Rev. B* **2020**, *102* (3), 035144.

(22) Hu, Y.; Xu, L.; Shi, M.; Luo, A.; Peng, S.; Wang, Z. Y.; Ying, J. J.; Wu, T.; Liu, Z. K.; Zhang, C. F.; Chen, Y. L.; Xu, G.; Chen, X.-H.; He, J.-F. Universal Gapless Dirac Cone and Tunable Topological States in $(MnBi_2Te_4)_m(Bi_2Te_3)_n$ Heterostructures. *Phys. Rev. B* **2020**, *101* (16), 161113.

(23) Klimovskikh, I. I.; Otrokov, M. M.; Estyunin, D.; Eremeev, S. V.; Filnov, S. O.; Koroleva, A.; Shevchenko, E.; Voroshnin, V.; Rybkin, A. G.; Rusinov, I. P.; Blanco-Rey, M.; Hoffmann, M.; Aliev, Z.

S.; Babanly, M. B.; Amiraslanov, I. R.; Abdullayev, N. A.; Zverev, V. N.; Kimura, A.; Tereshchenko, O. E.; Kokh, K. A.; Petaccia, L.; Di Santo, G.; Ernst, A.; Echenique, P. M.; Mamedov, N. T.; Shikin, A. M.; Chulkov, E. V. Tunable 3D/2D Magnetism in the $(MnBi_2Te_4)$-$(Bi_2Te_3)_m$ Topological Insulators Family. *Npj Quantum Mater.* **2020**, *5* (1), 54.

(24) Lu, R.; Sun, H.; Kumar, S.; Wang, Y.; Gu, M.; Zeng, M.; Hao, Y.-J.; Li, J.; Shao, J.; Ma, X.-M.; Hao, Z.; Zhang, K.; Mansuer, W.; Mei, J.; Zhao, Y.; Liu, C.; Deng, K.; Huang, W.; Shen, B.; Shimada, K.; Schwier, E. F.; Liu, C.; Liu, Q.; Chen, C. Half-Magnetic Topological Insulator with Magnetization-Induced Dirac Gap at a Selected Surface. *Phys. Rev. X* **2021**, *11* (1), 011039.

(25) Hu, C.; Ding, L.; Gordon, K. N.; Ghosh, B.; Tien, H.-J.; Li, H.; Linn, A. G.; Lien, S.-W.; Huang, C.-Y.; Mackey, S.; Liu, J.; Reddy, P. V. S.; Singh, B.; Agarwal, A.; Bansil, A.; Song, M.; Li, D.; Xu, S.-Y.; Lin, H.; Cao, H.; Chang, T.-R.; Dessau, D.; Ni, N. Realization of an Intrinsic Ferromagnetic Topological State in $MnBi_8Te_{13}$. *Sci. Adv.* **2020**, *6* (30), No. eaba4275.

(26) Souchay, D.; Nentwig, M.; Günther, D.; Keilholz, S.; de Boor, J.; Zeugner, A.; Isaeva, A.; Ruck, M.; Wolter, A. U.; Büchner, B.; Oeckler, O. Layered Manganese Bismuth Tellurides with $GeBi_4Te_7$ and $GeBi_6Te_{10}$ Type Structures: Towards Multifunctional Materials. *J. Mater. Chem. C* **2019**, *7* (32), 9939−9953.

(27) Shao, J.; Liu, Y.; Zeng, M.; Li, J.; Wu, X.; Ma, X.-M.; Jin, F.; Lu, R.; Sun, Y.; Gu, M.; Wang, K.; Wu, W.; Wu, L.; Liu, C.; Liu, Q.; Zhao, Y. Pressure-Tuned Intralayer Exchange in Superlattice-Like $MnBi_2Te_4/(Bi_2Te_3)_n$ Topological Insulators. *Nano Lett.* **2021**, *21* (13), 5874−5880.

(28) Liu, Y.; Wang, L.-L.; Zheng, Q.; Huang, Z.; Wang, X.; Chi, M.; Wu, Y.; Chakoumakos, B. C.; McGuire, M. A.; Sales, B. C.; Wu, W.; Yan, J. Site Mixing for Engineering Magnetic Topological Insulators. *Phys. Rev. X* **2021**, *11* (2), 021033.

(29) Murakami, T.; Nambu, Y.; Koretsune, T.; Xiangyu, G.; Yamamoto, T.; Brown, C. M.; Kageyama, H. Realization of Interlayer Ferromagnetic Interaction in $MnSb_2Te_4$ toward the Magnetic Weyl Semimetal State. *Phys. Rev. B* **2019**, *100* (19), 195103.

(30) Hou, F.; Yao, Q.; Zhou, C.-S.; Ma, X.-M.; Han, M.; Hao, Y.-J.; Wu, X.; Zhang, Y.; Sun, H.; Liu, C.; Zhao, Y.; Liu, Q.; Lin, J. Te-Vacancy-Induced Surface Collapse and Reconstruction in Antiferromagnetic Topological Insulator $MnBi_2Te_4$. *ACS Nano* **2020**, *14* (9), 11262−11272.

(31) Huang, Z.; Du, M.-H.; Yan, J.; Wu, W. Native Defects in Antiferromagnetic Topological Insulator $MnBi_2Te_4$. *Phys. Rev. Mater.* **2020**, *4* (12), 121202.

(32) Lai, Y.; Ke, L.; Yan, J.; McDonald, R. D.; McQueeney, R. J. Defect-Driven Ferrimagnetism and Hidden Magnetization in $MnBi_2Te_4$. *Phys. Rev. B* **2021**, *103* (18), 184429.

(33) Du, M.-H.; Yan, J.; Cooper, V. R.; Eisenbach, M. Tuning Fermi Levels in Intrinsic Antiferromagnetic Topological Insulators $MnBi_2Te_4$ and $MnBi_4Te_7$ by Defect Engineering and Chemical Doping. *Adv. Funct. Mater.* **2021**, *31* (3), 2006516.

(34) Hu, C.; Lien, S.-W.; Feng, E.; Mackey, S.; Tien, H.-J.; Mazin, I. I.; Cao, H.; Chang, T.-R.; Ni, N. Tuning Magnetism and Band Topology through Antisite Defects in Sb-Doped $MnBi_4Te_7$. *Phys. Rev. B* **2021**, *104* (5), 054422.

(35) Chen, L.; Wang, D.; Shi, C.; Jiang, C.; Liu, H.; Cui, G.; Zhang, X.; Li, X. Electronic Structure and Magnetism of MnSb2Te4. *J. Mater. Sci.* **2020**, *55* (29), 14292−14300.

(36) Wimmer, S.; Sánchez-Barriga, J.; Küppers, P.; Ney, A.; Schierle, E.; Freyse, F.; Caha, O.; Michalička, J.; Liebmann, M.; Primetzhofer, D.; Hoffman, M.; Ernst, A.; Otrokov, M. M.; Bihlmayer, G.; Weschke, E.; Lake, B.; Chulkov, E. V.; Morgenstern, M.; Bauer, G.; Springholz, G.; Rader, O. Mn-Rich $MnSb_2Te_4$: A Topological Insulator with Magnetic Gap Closing at High Curie Temperatures of 45−50 K. *Adv. Mater.* **2021**, *33* (42), 2102935.

(37) Guan, Y. D.; Yan, C. H.; Lee, S. H.; Gui, X.; Ning, W.; Ning, J. L.; Zhu, Y. L.; Kothakonda, M.; Xu, C. Q.; Ke, X. L.; Sun, J. W.; Xie, W. W.; Yang, S. L.; Mao, Z. Q. Ferromagnetic $MnBi_4Te_7$ Obtained with Low-Concentration Sb Doping: A Promising Platform for

Exploring Topological Quantum States. *Phys. Rev. Mater.* **2022**, *6* (5), 054203.

(38) Xie, H.; Wang, D.; Cai, Z.; Chen, B.; Guo, J.; Naveed, M.; Zhang, S.; Zhang, M.; Wang, X.; Fei, F.; Zhang, H.; Song, F. The Mechanism Exploration for Zero-Field Ferromagnetism in Intrinsic Topological Insulator $MnBi_2Te_4$ by Bi_2Te_3 Intercalations. *Appl. Phys. Lett.* **2020**, *116* (22), 221902.

(39) Aliev, Z. S.; Amiraslanov, I. R.; Nasonova, D. I.; Shevelkov, A. V.; Abdullayev, N. A.; Jahangirli, Z. A.; Orujlu, E. N.; Otrokov, M. M.; Mamedov, N. T.; Babanly, M. B.; Chulkov, E. V. Novel Ternary Layered Manganese Bismuth Tellurides of the $MnTe-Bi_2Te_3$ System: Synthesis and Crystal Structure. *J. Alloys Compd.* **2019**, *789*, 443−450.

(40) Ma, X.-M.; Chen, Z.; Schwier, E. F.; Zhang, Y.; Hao, Y.-J.; Kumar, S.; Lu, R.; Shao, J.; Jin, Y.; Zeng, M.; Liu, X.-R.; Hao, Z.; Zhang, K.; Mansuer, W.; Song, C.; Wang, Y.; Zhao, B.; Liu, C.; Deng, K.; Mei, J.; Shimada, K.; Zhao, Y.; Zhou, X.; Shen, B.; Huang, W.; Liu, C.; Xu, H.; Chen, C. Hybridization-Induced Gapped and Gapless States on the Surface of Magnetic Topological Insulators. *Phys. Rev. B* **2020**, *102* (24), 245136.

(41) Hu, C.; Tanatar, M. A.; Prozorov, R.; Ni, N. Unusual Dynamic Susceptibility Arising from Soft Ferromagnetic Domains in $MnBi_8Te_{13}$ and Sb-Doped $MnBi_{2n}Te_{3n+1}$ ($n = 2, 3$). *J. Phys. Appl. Phys.* **2022**, *55* (5), 054003.

(42) Wu, X.; Li, J.; Ma, X.-M.; Zhang, Y.; Liu, Y.; Zhou, C.-S.; Shao, J.; Wang, Q.; Hao, Y.-J.; Feng, Y.; Schwier, E. F.; Kumar, S.; Sun, H.; Liu, P.; Shimada, K.; Miyamoto, K.; Okuda, T.; Wang, K.; Xie, M.; Chen, C.; Liu, Q.; Liu, C.; Zhao, Y. Distinct Topological Surface States on the Two Terminations of $MnBi_4Te_7$. *Phys. Rev. X* **2020**, *10* (3), 031013.

(43) Vidal, R. C.; Bentmann, H.; Facio, J. I.; Heider, T.; Kagerer, P.; Fornari, C. I.; Peixoto, T. R. F.; Figgemeier, T.; Jung, S.; Cacho, C.; Büchner, B.; van den Brink, J.; Schneider, C. M.; Plucinski, L.; Schwier, E. F.; Shimada, K.; Richter, M.; Isaeva, A.; Reinert, F. Orbital Complexity in Intrinsic Magnetic Topological Insulator $MnBi_4Te_7$ and $MnBi_6Te_{10}$. *Phys. Rev. Lett.* **2021**, *126* (17), 176403.

(44) Jo, N. H.; Wang, L.-L.; Slager, R.-J.; Yan, J.; Wu, Y.; Lee, K.; Schrunk, B.; Vishwanath, A.; Kaminski, A. Intrinsic Axion Insulating Behavior in Antiferromagnetic $MnBi_6Te_{10}$. *Phys. Rev. B* **2020**, *102* (4), 045130.

(45) Gordon, K. N.; Sun, H.; Hu, C.; Linn, A. G.; Li, H.; Liu, Y.; Liu, P.; Mackey, S.; Liu, Q.; Ni, N.; Dessau, D.Strongly Gapped Topological Surface States on Protected Surfaces of Antiferromagnetic $MnBi_4Te_7$ and $MnBi_6Te_{10}$. **2019**, 1910.13943. *arXiv*. DOI: 10.48550/arXiv.1910.13943 (accessed June 24, 2022).

(46) Tan, H.; Yan, B.Distinct Magnetic Gaps between Antiferromagnetic and Ferromagnetic Orders Driven by Surface Defects in the Topological Magnet MnBi2Te4. **2022**, 2207.13511. *arXiv*. DOI: 10.48550/arXiv.2207.13511 (accessed September 08, 2022).

(47) Garnica, M.; Otrokov, M. M.; Aguilar, P. C.; Klimovskikh, I. I.; Estyunin, D.; Aliev, Z. S.; Amiraslanov, I. R.; Abdullayev, N. A.; Zverev, V. N.; Babanly, M. B.; Mamedov, N. T.; Shikin, A. M.; Arnau, A.; de Parga, A. L. V.; Chulkov, E. V.; Miranda, R. Native Point Defects and Their Implications for the Dirac Point Gap at $MnBi_2Te_4$(0001). *Npj Quantum Mater.* **2022**, *7* (1), 1−9.

(48) Shikin, A. M.; Estyunin, D. A.; Klimovskikh, I. I.; Filnov, S. O.; Schwier, E. F.; Kumar, S.; Miyamoto, K.; Okuda, T.; Kimura, A.; Kuroda, K.; Yaji, K.; Shin, S.; Takeda, Y.; Saitoh, Y.; Aliev, Z. S.; Mamedov, N. T.; Amiraslanov, I. R.; Babanly, M. B.; Otrokov, M. M.; Eremeev, S. V.; Chulkov, E. V. Nature of the Dirac Gap Modulation and Surface Magnetic Interaction in Axion Antiferromagnetic Topological Insulator $MnBi_2Te_4$. *Sci. Rep.* **2020**, *10* (1), 13226.

(49) Ma, X.-M.; Zhao, Y.; Zhang, K.; Kumar, S.; Lu, R.; Li, J.; Yao, Q.; Shao, J.; Hou, F.; Wu, X.; Zeng, M.; Hao, Y.-J.; Hao, Z.; Wang, Y.; Liu, X.-R.; Shen, H.; Sun, H.; Mei, J.; Miyamoto, K.; Okuda, T.; Arita, M.; Schwier, E. F.; Shimada, K.; Deng, K.; Liu, C.; Lin, J.; Zhao, Y.; Chen, C.; Liu, Q.; Liu, C. Realization of a Tunable Surface Dirac Gap in Sb-Doped $MnBi_2Te_4$. *Phys. Rev. B* **2021**, *103* (12), L121112.

(50) Shikin, A. M.; Estyunin, D. A.; Zaitsev, N. L.; Glazkova, D.; Klimovskikh, I. I.; Filnov, S. O.; Rybkin, A. G.; Schwier, E. F.; Kumar, S.; Kimura, A.; Mamedov, N.; Aliev, Z.; Babanly, M. B.; Kokh, K.; Tereshchenko, O. E.; Otrokov, M. M.; Chulkov, E. V.; Zvezdin, K. A.; Zvezdin, A. K. Sample-Dependent Dirac-Point Gap in $MnBi_2Te_4$ and Its Response to Applied Surface Charge: A Combined Photoemission and Ab Initio Study. *Phys. Rev. B* **2021**, *104* (11), 115168.

(51) Hor, Y. S.; Roushan, P.; Beidenkopf, H.; Seo, J.; Qu, D.; Checkelsky, J. G.; Wray, L. A.; Hsieh, D.; Xia, Y.; Xu, S.-Y.; Qian, D.; Hasan, M. Z.; Ong, N. P.; Yazdani, A.; Cava, R. J. Development of Ferromagnetism in the Doped Topological Insulator Bi_2Te_3. *Phys. Rev. B* **2010**, *81* (19), 195203.

(52) Lee, J. S.; Richardella, A.; Rench, D. W.; Fraleigh, R. D.; Flanagan, T. C.; Borchers, J. A.; Tao, J.; Samarth, N. Ferromagnetism and Spin-Dependent Transport in n-Type Mn-Doped Bismuth Telluride Thin Films. *Phys. Rev. B* **2014**, *89* (17), 174425.

(53) Vobornik, I.; Panaccione, G.; Fujii, J.; Zhu, Z.-H.; Offi, F.; Salles, B. R.; Borgatti, F.; Torelli, P.; Rueff, J. P.; Ceolin, D.; Artioli, A.; Unnikrishnan, M.; Levy, G.; Marangolo, M.; Eddrief, M.; Krizmancic, D.; Ji, H.; Damascelli, A.; van der Laan, G.; Egdell, R. G.; Cava, R. J. Observation of Distinct Bulk and Surface Chemical Environments in a Topological Insulator under Magnetic Doping. *J. Phys. Chem. C* **2014**, *118* (23), 12333−12339.

(54) Teng, J.; Liu, N.; Li, Y. Mn-Doped Topological Insulators: A Review. *J. Semicond.* **2019**, *40* (8), 081507.

(55) Chen, B.; Wang, D.; Jiang, Z.; Zhang, B.; Cui, S.; Guo, J.; Xie, H.; Zhang, Y.; Naveed, M.; Du, Y.; Wang, X.; Zhang, H.; Fei, F.; Shen, D.; Sun, Z.; Song, F. Coexistence of Ferromagnetism and Topology by Charge Carrier Engineering in the Intrinsic Magnetic Topological Insulator $Mn Bi_4Te_7$. *Phys. Rev. B* **2021**, *104* (7), 075134.

(56) Sitnicka, J.; Park, K.; Skupiński, P.Ł; Grasza, K.; Reszka, A.; Sobczak, K.; Borysiuk, J.; Adamus, Z.; Tokarczyk, M.; Avdonin, A.; Fedorchenko, I.; Abałoszewa, I.; Turczyniak-Surdacka, S.; Olszowska, N.; Kołodziej, J.; Kowalski, B. J; Deng, H.; Konczykowski, M.; Krusin-Elbaum, L.; Wołoś, A. Systemic Consequences of Disorder in Magnetically Self-Organized Topological $MnBi_2Te_4/(Bi_2Te_3)_n$ Superlattices. *2D Mater.* **2022**, *9* (1), 015026.

(57) Yan, C.; Green, E.; Fukumori, R.; Protic, N.; Lee, S. H.; Fernandez-Mulligan, S.; Raja, R.; Erdakos, R.; Mao, Z.; Yang, S. An Integrated Quantum Material Testbed with Multi-Resolution Photo-emission Spectroscopy. *Rev. Sci. Instrum.* **2021**, *92* (11), 113907.